

This is an electronic reprint of the original article. This reprint may differ from the original in pagination and typographic detail.

A pH-Responsive Cluster Metal–Organic Framework Nanoparticle for Enhanced Tumor Accumulation and Antitumor Effect

Cheng, Ruoyu; Jiang, Lingxi; Gao, Han; Liu, Zehua; Mäkilä, Ermei; Wang, Shiqi; Saiding, Qimanguli; Xiang, Lei; Tang, Xiaomei; Shi, Minmin; Liu, Jia; Pang, Libin; Salonen, Jarno; Hirvonen, Jouni; Zhang, Hongbo; Cui, Wenguo; Shen, Baiyong; Santos, Hélder A.

Published in:
Advanced Materials

DOI:
[10.1002/adma.202203915](https://doi.org/10.1002/adma.202203915)

Published: 01/10/2022

Document Version
Final published version

Document License
CC BY

[Link to publication](#)

Please cite the original version:

Cheng, R., Jiang, L., Gao, H., Liu, Z., Mäkilä, E., Wang, S., Saiding, Q., Xiang, L., Tang, X., Shi, M., Liu, J., Pang, L., Salonen, J., Hirvonen, J., Zhang, H., Cui, W., Shen, B., & Santos, H. A. (2022). A pH-Responsive Cluster Metal–Organic Framework Nanoparticle for Enhanced Tumor Accumulation and Antitumor Effect. *Advanced Materials*, 34(42), Article 2203915. <https://doi.org/10.1002/adma.202203915>

General rights

Copyright and moral rights for the publications made accessible in the public portal are retained by the authors and/or other copyright owners and it is a condition of accessing publications that users recognise and abide by the legal requirements associated with these rights.

Take down policy

If you believe that this document breaches copyright please contact us providing details, and we will remove access to the work immediately and investigate your claim.

A pH-Responsive Cluster Metal–Organic Framework Nanoparticle for Enhanced Tumor Accumulation and Antitumor Effect

Ruoyu Cheng, Lingxi Jiang, Han Gao, Zehua Liu, Ermei Mäkilä, Shiqi Wang, Qimanguli Saiding, Lei Xiang, Xiaomei Tang, Minmin Shi, Jia Liu, Libin Pang, Jarno Salonen, Jouni Hirvonen, Hongbo Zhang, Wenguo Cui,* Baiyong Shen,* and Hélder A. Santos*

As a result of the deficient tumor-specific antigens, potential off-target effect, and influence of protein corona, metal–organic framework nanoparticles have inadequate accumulation in tumor tissues, limiting their therapeutic effects. In this work, a pH-responsive linker (L) is prepared by covalently modifying oleylamine (OA) with 3-(bromomethyl)-4-methyl-2,5-furandione (MMfu) and poly(ethylene glycol) (PEG). Then, the L is embedded into a solid lipid nanoshell to coat apilimod (Ap)-loaded zeolitic imidazolate framework (Ap-ZIF) to form Ap-ZIF@SLN#L. Under the tumor microenvironment, the hydrophilic PEG and MMfu are removed, exposing the hydrophobic OA on Ap-ZIF@SLN#L, increasing their uptake in cancer cells and accumulation in the tumor. The ZIF@SLN#L nanoparticle induces reactive oxygen species (ROS). Ap released from Ap-ZIF@SLN#L significantly promotes intracellular ROS and lactate dehydrogenase generation. Ap-ZIF@SLN#L inhibits tumor growth, increases the survival rate in mice, activates the tumor microenvironment, and improves the infiltration of macrophages and T cells in the tumor, as demonstrated in two different tumor-bearing mice after injections with Ap-ZIF@SLN#L. Furthermore, mice show normal tissue structure of the main organs and the normal serum level in alanine aminotransferase and aspartate aminotransferase after treatment with the nanoparticles. Overall, this pH-responsive targeting strategy improves nanoparticle accumulation in tumors with enhanced therapeutic effects.

1. Introduction

Metal–organic frameworks (MOFs), crystalline hybrid materials built up from the coordination between metal (transition metal or lanthanide metal) ions and organic ligands (carboxylates, azolates, and phosphonates), exhibit controlled surface chemistry, unparalleled surface areas, and pore volumes, and reversible structural flexibility.^[1–3] These properties make MOFs an outstanding candidate for drug delivery and biomedical applications.^[4–6] For example, drugs with different properties, such as hydrophobic and hydrophilic drugs, and proteins, can be effectively loaded into MOFs;^[7,8] easily tailored properties mean that MOFs can be modified by different ligands, such as peptides and fluorescence, for various applications.^[9,10] Due to these advantages, previous studies have focused on exploring the potential capability of MOFs in cancer treatments.^[11] However, there are still some challenges in applying MOFs for cancer therapy. For example, during the formation of the

R. Cheng, L. Jiang, X. Tang, M. Shi, J. Liu, B. Shen
Department of General Surgery
Pancreatic Disease Center
Ruijin Hospital
Shanghai Jiao Tong University School of Medicine
197 Ruijin Second Road, Shanghai 200025, P. R. China
E-mail: shenby@shsmu.edu.cn

 The ORCID identification number(s) for the author(s) of this article can be found under <https://doi.org/10.1002/adma.202203915>.

© 2022 The Authors. Advanced Materials published by Wiley-VCH GmbH. This is an open access article under the terms of the Creative Commons Attribution-NonCommercial License, which permits use, distribution and reproduction in any medium, provided the original work is properly cited and is not used for commercial purposes.

R. Cheng, H. Gao, H. A. Santos
Department of Biomedical Engineering
W.J. Korf Institute for Biomedical Engineering and Materials Science
University Medical Center Groningen/University of Groningen
Groningen 9713 AV, The Netherlands
E-mail: h.a.santos@umcg.nl

R. Cheng, Q. Saiding, L. Xiang, L. Pang, H. Zhang, W. Cui, H. A. Santos
Department of Orthopaedics, Shanghai Key Laboratory for Prevention and Treatment of Bone and Joint Diseases
Shanghai Institute of Traumatology and Orthopaedics
Ruijin Hospital
Shanghai Jiao Tong University School of Medicine
197 Ruijin 2nd Road, Shanghai 200025, P. R. China
E-mail: wgcai@sjtu.edu.cn

DOI: 10.1002/adma.202203915

MOF, homogeneous nucleation first excessively appears.^[12] If the unreacted precursors cannot be rapidly depleted, the generated nucleus will continuously grow, generating microparticles rather than nanoparticles.^[13] These microparticles usually exhibit limited accumulation in the tumor tissues compared to the nanoparticles by intravenous injection. Although MOFs are fabricated by coordinating metal ions and organic ligands, massive ions and proteins in the circulation system will also interact with the metal ions or organic ligands of the MOF, causing unforeseen degradation or aggradation before the MOF arrives at the destination.^[14] Therefore, developing a strategy to increase MOF nanoparticle accumulation in tumor tissues would be necessary to achieve enhanced therapeutic effects.

Works have shown the development of various strategies to improve MOF nanoparticle accumulation in tumors.^[15,16] Active targeting is one of the most popular strategies for raising the concentration of nanoparticles or drugs in tumor tissues.^[17,18] Tumor-associated antigens (TAAs) or tumor-specific antigens (TSAs) are commonly used as specific targets for the nanoparticles to interact with their functional targeting ligands.^[19,20] However, these active targeting strategies are limited by the deficient TSAs or TAAs on some incredibly immune-suppressive solid tumors, such as pancreatic and triple-negative breast cancers.^[21,22] These active targeting nanoparticles can also suffer from surface protein corona formation or off-target effects when injected inside the body. Therefore, developing other potential targeting strategies that can increase the accumulation of MOF nanoparticles or drugs in tumor tissues more effectively is highly demanded.

The tumor microenvironment (TME) has the loose structure of epithelial cells that causes the leaking and accumulating of contents from the blood flow to a greater extent than in normal tissue. It has been indicated that nanoparticles of a specific size (usually <200 nm) can pass through the loose epithelial cells and arrive at the tumor tissues.^[23] In addition, the pH in tumor tissues is lower than in normal tissues, attributing to the production of numerous lactates and excess protons of carbon dioxide by the glycolysis of cancer cells, which is commonly

found in most solid tumors.^[24,25] Therefore, these characteristics of TME can be utilized to develop pH-responsive nanoparticles or drugs to increase their accumulation in tumor tissues.

Considering the acidic TME condition and loose structure of epithelial cells, a pH-responsive cluster MOF nanoparticle is designed to enhance its accumulation in tumors and improve the therapeutic effects in this work. The hydrophobic oleylamine (OA) was covalently modified with hydrophilic poly(ethylene glycol) (PEG) by a pH-sensitive traceless linker 3-(bromomethyl)-4-methyl-2,5-furandione (MMfu) to prepare the pH-responsive linker (L). A similar carbon chain to 1,2-distearoyl-sn-glycero-3-phosphoethanolamine (mPEG-DSPE) turns L into partially hydrophobic. The zeolitic imidazolate framework (ZIF) was used as a typical MOF nanoparticle for drug loading and inducing the reactive oxygen species (ROS) generation, and apilimod (Ap) was used as a model drug to inhibit the autophagy capability since the cancer cells usually have a higher autophagy level than the normal cells. Microfluidics was used to coat the Ap-loaded ZIF with the solid lipid nanoshell containing L (Ap-ZIF@SLN#L), as shown in **Scheme 1**. It is hypothesized that the Ap-ZIF@SLN#L can homogeneously distribute in physiological conditions (pH 7.4) and expose the hydrophobic OA part under the acid condition (pH 6.0), leading to the formation of clustering nanoparticles with increased tumor accumulation in vivo and in vitro. Consequently, the clustering nanoparticles may increase ROS generation under the induction by the ZIF@SLN#L and the autophagy inhibition caused by the Ap, causing the inhibition of the proliferation of cancer cells and activated TME.

2. Results and Discussion

One of the most promising techniques, microfluidics, was used to precisely prepare the TME targeting cluster nanoparticles on a glass microchip. Typically, the formation of nanoparticles is based on the classical nucleation theory, and a specific supersaturation status is induced by the rapidly increased free monomers concentration in solution.^[12,26] Then energy barrier for nucleation is overcome, leading to the burst nucleation. Furthermore, the burst nucleation decreases the supersaturation status shutting down the nucleation. Additionally, nucleation is related to the formation of nanoparticles. The nucleation rate is positively correlated to the nuclei density, resulting in smaller nanoparticles and enhanced particle yield. However, the bulk method fails to create a homogenous condition within the orders of milliseconds, which could cause the inhomogeneous concentration of monomers, further leading to the higher batch-to-batch variation.^[27,28] Microfluidic can effectively mix the monomers and create a homogeneous status, decreasing the batch-to-batch variation.^[29,30] Before fabricating the nanoparticles, the compositions were first optimized. Since the zinc nitrate hexahydrate and 2-methylimidazole synthesized ZIF, a series of amounts and ratios between the two chemicals were used to prepare various ZIF (denoted as ZIF1-14), and the properties of ZIF1-14 were evaluated by the dynamic light scattering (DLS). Comparing the counting rate (Figure S1A,B, Supporting Information) and hydrodynamic diameter (**Figure 1A,B**) of ZIF1-14 after synthesis and after 24 h,

R. Cheng, H. Gao, Z. Liu, S. Wang, J. Hirvonen, H. A. Santos
Drug Research Program

Division of Pharmaceutical Chemistry and Technology

Faculty of Pharmacy

University of Helsinki

Helsinki FI-00014, Finland

E. Mäkilä, J. Salonen

Laboratory of Industrial Physics

Department of Physics

University of Turku

Turku FI-20014, Finland

H. Zhang

Pharmaceutical Sciences Laboratory

Åbo Akademi University

Turku FI-20520, Finland

H. Zhang

Turku Biosciences Center

University of Turku and Åbo Akademi University

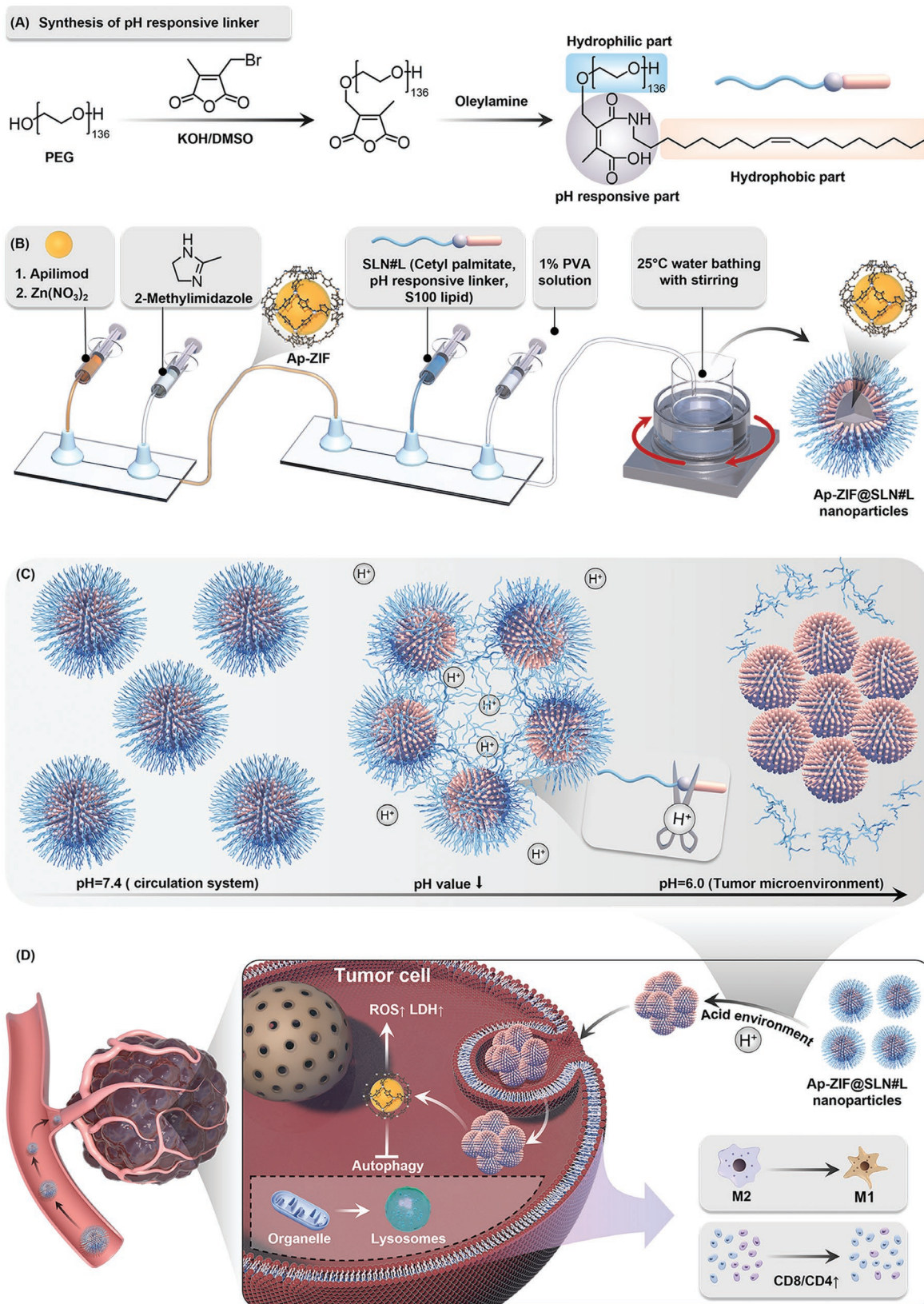
Turku FI-20520, Finland

L. Jiang, X. Tang, M. Shi, J. Liu, B. Shen

Research Institute of Pancreatic Diseases

Shanghai Jiaotong University School of Medicine

197 Ruijin 2nd Road, Shanghai 200025, China



Scheme 1. Schematic illustration of the underlying nanoparticle fabrication and therapeutic concept. A) Synthesis of the pH-responsive linker consisting of PEG, MMfu, and OA parts. B) The Ap-ZIF@SLN#L nanoparticles were prepared by a series connection between two chips. C) Hypothetic mechanism of the pH-responsive cluster Ap-ZIF@SLN#L nanoparticle. D) Hypothetic mechanism of the therapeutic effect caused by the Ap-ZIF@SLN#L nanoparticles.

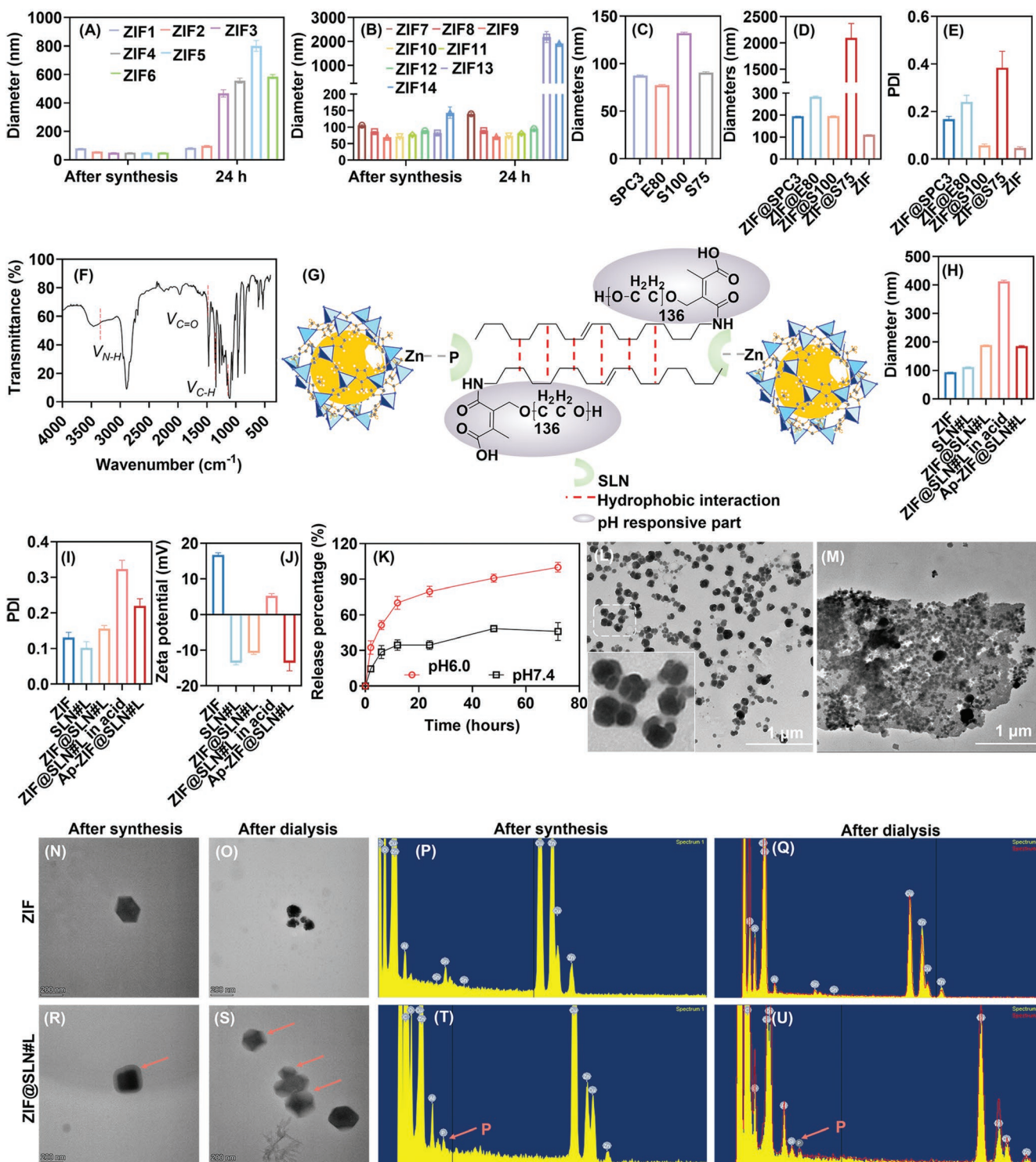


Figure 1. Preparation and characterization of the nanoparticles. A,B Evaluating the ZIF prepared by different amounts (A) and ratios (B) of the zinc nitrate hexahydrate and 2-methylimidazole in the hydrodynamic size diameter. C) Evaluating the size of the SLN nanoparticles prepared with four different lipids, SPC3, E80, S100, and S75. D,E Investigating the ZIF coated with SLN prepared with four different lipids, SPC3, E80, S100, and S75, in terms of hydrodynamic size diameter (D) and PDI (E). F) FTIR spectrum of the pH-responsive linker. G) Schematic illustration of the interaction among nanoparticles. H–J) Investigating the properties of various nanoparticles in terms of hydrodynamic size diameter (H), PDI (I), and zeta-potential (J). K) The drug release behavior of Ap-ZIF@SLN#L in pH 6.0 and 7.4. L,M) TEM images of ZIF@SLN#L in PBS (pH 7.4) (L), with the local magnification image inset with a white circle, and at pH 6.0 (M). N–Q) TEM images and EDX analyses of ZIF after synthesis (N,P) and after dialysis (O,Q). R–U) TEM images and EDX analyses of ZIF@SLN#L after synthesis (R,T) and after dialysis (S,U). Error bars are based on standard errors of the mean ($n = 3$).

the amount and ratio of zinc nitrate hexahydrate and 2-methylimidazole were fixed at 9.27 mg mL⁻¹, and 1:10. Limiting by the unsatisfactory stability of bare ZIF in physiological conditions,^[31,32] a composite solid lipid structure was coated on the ZIF to improve the stability and fabricate the pH-responsive cluster nanoparticles. Supporting by previous studies, elements in lipid, such as phosphorus and choline, could interact with zinc.^[33,34] We hypothesized that this interaction could contribute to forming a solid lipid nanoshell (SLN) on the ZIF. Therefore, four different lipids, soy phosphatidylcholine (SPC3, S100, and S75), and egg phospholipid (E80) were first mixed with cetyl palmitate and 1,2-distearoyl-sn-glycero-3-phosphoethanolamine (mPEG-DSPE) to prepare the solid lipid nanoparticles without ZIF (denoted as SPC3, E80, S100, and S75). S100 is 100% phosphatidylcholine, and S75 is 70% phosphatidylcholine; both S100 and S75 come from soybean. E80 comes from the egg with 80% phosphatidylcholine. SPC3 also comes from soybean with pure phosphatidylcholine and iodine value of 3. The structure of phosphatidylcholine was exhibited in Figure S1C, (Supporting Information). In addition, ZIF coated with these four different lipids was prepared (ZIF@SPC3, ZIF@E80, ZIF@S100, and ZIF@S75). The nanoparticles' hydrodynamic diameter and polydispersity index (PDI) were investigated to evaluate which lipid was more promising in forming the SLN on the ZIF. The hydrodynamic diameter of SPC3, E80, S100, and S75 was respectively at 87.6 ± 0.6, 77.3 ± 0.7, 132.2 ± 1.0, and 90.8 ± 0.8 nm (Figure 1C), and ZIF@SPC3 (194.9 ± 0.6 nm, PDI: 0.168 ± 0.01), ZIF@E80 (283.8 ± 3.5 nm, PDI: 0.241 ± 0.03), ZIF@S100 (195.9 ± 1.3 nm, PDI: 0.06 ± 0.01), ZIF@S75 (2096.3 ± 276.3 nm, PDI: 0.384 ± 0.07), and ZIF (111.2 ± 0.4 nm, PDI: 0.05 ± 0.01) (Figure 1D,E). There was an increased hydrodynamic diameter from S100 (132.2 ± 1.0 nm) to ZIF@S100 (195.9 ± 1.3 nm) with uniform distribution (PDI: 0.06 ± 0.01) compared to the ZIF coated with the other three lipids, which indicates the S100 is a more promising lipid in forming the SLN on the ZIF.

After optimizing the compositions, a pH-responsive linker (denoted as L) was synthesized. The PEG chains were first connected with the 3-(bromomethyl)-4-methyl-2,5-furandione (MMfu), followed by connected with OA. The PEG chains were regarded as a hydrophilic part, and OA was the hydrophobic part. These two parts were connected by a pH-responsive trackless removable compound MMfu.^[35] The final product was investigated by Fourier transform infrared (FTIR) spectroscopy (Figure 1F). The stretching vibration of N–H, ≈3500 cm⁻¹, the stretching vibration of C=O, ≈1680 cm⁻¹, the stretching vibration of C–N, ≈1264 cm⁻¹, and the deformation vibration of N–H, ≈1538 cm⁻¹, confirmed the formation of the amide bond, suggesting the successful synthesis of the tumor environment targeting linker. Additionally, the PEG, MMfu, and linker were also investigated by the ¹H nuclear magnetic resonance (¹H NMR, Figure S2A–C, Supporting Information). The (3.5–4.0 ppm) were the vibration absorption peaks of –CH₂– on PEG; b (2.09 ppm) and c (4.46 ppm) were the vibration absorption peaks of –CH₃– and –CH₂–Br on MMfu; d (7.0 ppm), e (0.7–2.7 ppm) were the vibration absorption peaks of –CH₂=CH₂– and –CH₂– on OA; the ¹H NMR results further proved the successful synthesis of the linker. As shown in Figure 1G, the Zn on the ZIF interacts with P on the S100 to enhance the coating

efficiency; After removing the pH-responsive part, the OA on the surface of nanoparticles has a hydrophobic interaction leading to the clustering of nanoparticles. Afterward, ZIF, SLN containing the pH-responsive linker (denoted as SLN#L), ZIF coated with SLN#L (denoted as ZIF@SLN#L), and apilimod (Ap)-loaded ZIF@SLN#L (denoted as Ap-ZIF@SLN#L) were prepared by the microfluidics for the following study. DLS first analyzed these nanoparticles regarding their hydrodynamic diameter, PDI, and zeta-potential. As shown in Figure 1H–J, an increase in the hydrodynamic size diameter and reversed zeta-potential were observed in the ZIF@SLN#L (189.4 ± 0.6 nm, –10.7 ± 0.5 mV) compared to the ZIF (94.0 ± 0.5 nm, 16.7 ± 0.6 mV), and the zeta-potential of SLN#L was –13.5 ± 0.6 mV. These results show the successful coating of SLN#L on ZIF. Additionally, the ZIF, ZIF@SLN, and Ap-ZIF@SLN#L were also investigated by the FTIR (Figure S1D–F, Supporting Information). The imidazolate ring stretching was observed from 1400–1500 cm⁻¹, and the C=N stretching (1584 cm⁻¹) proved the fabrication of ZIF. The broad bands from 1200–1500 cm⁻¹ could be attributed to the deformation of –CH₂–, and –CH₃–proving the coating of SLN. Furthermore, the C–H aliphatic stretching (2945 cm⁻¹) belonging to the cetyl palmitate was observed on the ZIF@SLN and ZIF@SLN#L. Moreover, the stretching vibration of N–H, ≈3500 cm⁻¹, proved the presence of L on Ap-ZIF@SLN#L. The ZIF, ZIF@SLN, and Ap-ZIF@SLN#L were investigated by X-ray diffraction (XRD, Figure S1G–I, Supporting Information), proving the changes in crystal structure after modifying the SLN and SLN#L with Ap. Thermogravimetric analysis (TGA, Figure S1J–L, Supporting Information) proved the successful preparation of ZIF, ZIF@SLN#L, and Ap-ZIF@SLN#L. With the addition of SLN and SLN#L with Ap, ZIF@SLN and Ap-ZIF@SLN#L exhibited different TG curves compared to the ZIF. A sharp weight decrease can be observed on ZIF at ≈500 °C compared to a broader TG curve on ZIF@SLN (from above 200 °C) and Ap-ZIF@SLN#L (from above 100 °C). Moreover, these nanoparticles were also tested in an acid environment. As a result, an increase in the hydrodynamic size diameters and PDI were observed for ZIF@SLN#L from 189.4 ± 0.6 nm and 0.156 ± 0.01 to 412.7 ± 3.8 nm and 0.323 ± 0.02, respectively, in acid solution (pH 6.0 to mimic the tumor microenvironment). Additionally, the Ap-ZIF@SLN#L showed similar properties (186 ± 1.6 nm, 0.220 ± 0.02, and –13.5 ± 2.3 mV) as ZIF@SLN#L, indicating no influence caused by the loading of Ap in the Ap-ZIF@SLN#L structure. Additionally, the drug release behavior of Ap-ZIF@SLN#L (Encapsulation efficiency: 81.2 ± 2.1%, loading efficiency: 10.9 ± 0.3%) was tested in both physiological and acidic pH; stable and burst drug release can be observed at different pH (Figure 1K and Figure S1M, Supporting Information).

TEM shows no apparent aggregation in ZIF@SLN#L in PBS (pH 7.4). However, the lipid coatings can be observed on the surface of ZIF in the locally magnified images, demonstrating the successful fabrication of the core-shell structure (Figure 1L). In contrast, large clustering nanoparticles can be observed in ZIF@SLN#L at pH 6.0 (Figure 1M), which indicates that under the tumor microenvironment, the MMfu and PEG can be tracklessly removed from the ZIF@SLN#L, leading to the exposure of the hydrophobic OA part and clustering nanoparticles. Besides, we also dialyzed the ZIF@SLN#L

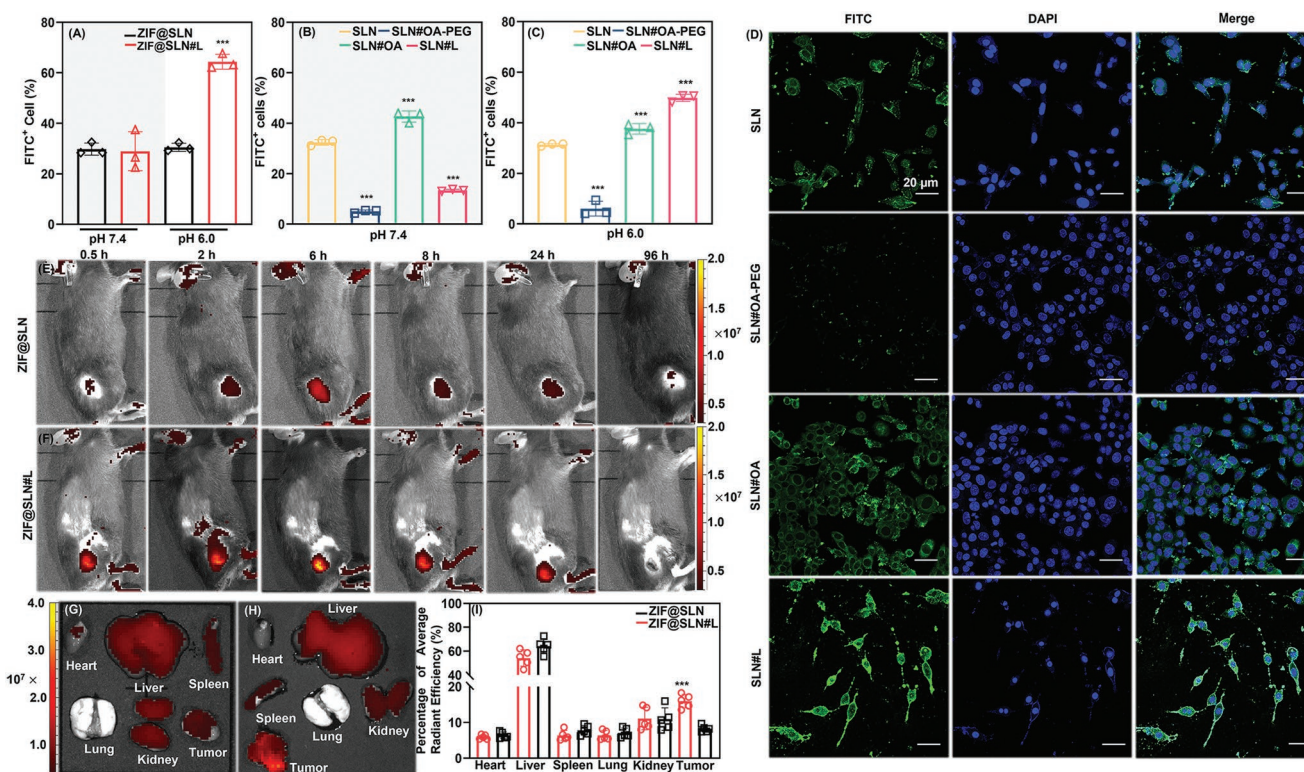


Figure 2. A) Flow cytometry results of the FITC⁺ Pan02 cells treated with ZIF@SLN or ZIF@SLN#L at pH 7.4 or pH 6.0. B,C) FITC⁺ Pan02 cells treated with SLN, SLN#OA, SLN#OA-PEG, and SLN#L at pH 7.4 (B), pH 6.0 (C), and D) confocal fluorescence microscopy images at pH 6.0 ($n = 3$). Scale bars: 20 μm . E,F) The time-dependent biodistribution of ZIF@SLN (E) and ZIF@SLN#L (F) after intravenous injection. G,H) Biodistribution of ZIF@SLN (G) and ZIF@SLN#L (H) in the main organs and tumor after 6 h post-intravenous injection, and I) quantitative analysis in the average radiant efficiency ($n = 5$). The error bars are based on standard errors of the individual animals ($n = 5$), $***p < 0.001$, analysis of variance (ANOVA) with Tukey's post-test.

and ZIF overnight to investigate the core-shell structure on ZIF@SLN#L. After synthesis, ZIF shows a regular hexagon-like structure (Figure 1N). However, most ZIF dissolved after dialysis without specific morphology (Figure 1O). In addition, there was no phosphorus element detected in ZIF before or after dialysis, according to the results of EDX analysis (Figure 1P,Q). By contrast, ZIF@SLN#L maintained specific morphology before and after dialysis (Figure 1R,X), which indicates the lipid coating structure of ZIF@SLN#L with improved nanoparticle stability in the solution. Moreover, the phosphorus element appeared in the EDX results before and after dialysis (Figure 1T,U), attributing to the presence of S100 on ZIF@SLN#L. Additionally, the hydrodynamic diameter and PDI of ZIF@SLN#L and ZIF were evaluated in different media during 2 h incubation (Figure S1N–Q, Supporting Information). Stable hydrodynamic size diameter and PDI were observed in the ZIF@SLN#L compared to the ZIF, indicating the successful coating of SLN#L on the ZIF. Overall, these results showed the successful fabrication of ZIF@SLN#L with potential pH-responsive capability.

Since ZIF@SLN#L can cluster in acid pH (6.0) (Figure 1M), we further explore the potential pH-responsive capability of ZIF@SLN#L both in vitro and in vivo. The ZIF@SLN and ZIF@SLN#L (labeled with coumarin-6 as a fluorescein isothiocyanate, FITC, marker) were cultured with Pan02 cells in a culture medium at pH 6.0 and 7.4 to study whether the cell culture medium with different pH-values can influence the cellular

uptake efficiency of the nanoparticles in vitro. The ZIF@SLN was used as control nanoparticles without the pH-responsive linker. After being quantified by flow cytometry, the cellular uptake efficiencies of ZIF@SLN ($29.7 \pm 2.4\%$) and ZIF@SLN#L ($28.9 \pm 7.7\%$) were similar at pH 7.4. Interestingly, the uptake efficiencies of ZIF@SLN#L increased to $64.4 \pm 2.9\%$ compared with the $30.5 \pm 1.6\%$ ZIF@SLN at pH 6.0 (Figure 2A). To eliminate the potential influence of nanoparticles adhered to cell membranes, trypan blue was used to quench the potential influence, followed by analysis with flow cytometry. The uptake efficiencies of ZIF@SLN#L and ZIF@SLN exhibited a similar trend as the unquenched data, indicating the internalization of the nanoparticles (Figure S1R, Supporting Information). To explore the potential mechanism of the increased cellular uptake of ZIF@SLN#L in Pan02 cells at pH 6.0, four nanoparticles, SLN, SLN modified with OA (SLN#OA), SLN modified with mPEG-DSPE and OA (SLN#OA-PEG), and SLN modified with pH-responsive linker (SLN#L), were prepared and cultured with Pan02 cells in culture medium (pH 7.4) (Figure 2B) and pH 6.0 (Figure 2C). All nanoparticles were labeled with coumarin-6 as a FITC marker, and flow cytometry was used to quantify the cellular uptake of the nanoparticles. The cellular uptake of SLN was $32.4 \pm 1.1\%$ and $31.3 \pm 0.5\%$ at pH 7.4 and 6.0, respectively, without statistically significant differences in the cellular uptake at the different pH values. The cellular uptake of SLN#OA was higher than that of SLN at pH 7.4 ($42.6 \pm 2.2\%$),

and 6.0 ($376 \pm 2.1\%$) without differences in cellular uptake at the studied pH values, indicating the modification of OA leads to the enhanced cellular uptake efficiency. The cellular uptake of SLN#OA-PEG was the lowest at pH 7.4 ($5.0 \pm 0.6\%$) and pH 6.0 ($6.0 \pm 2.9\%$) compared with the other three groups, which is attributed to the steric hindrance of PEG chains and the covering effect of PEG chains on the OA.^[36,37] In contrast, the cellular uptake of SLN#L was pH-dependent as $13.4 \pm 0.4\%$ for pH 7.4 and $49.8 \pm 1.4\%$ for pH 6.0. The cellular uptake of SLN#L was similar to that of SLN#OA-PEG at pH 7.4, which is attributed to the effects of the PEG's chains. However, the increased cellular uptake of SLN#L was observed at pH 6.0, which is attributed to the removing PEG chains and exposing OA to the acid environment. Furthermore, the Pan02 cells treated with four nanoparticles were observed by confocal fluorescence microscopy, and strong green fluorescence was observed around the nucleus of Pan02 cells cultured with SLN#L at pH 6.0 (Figure 2D). These results indicated that the pH-responsive linker could tracklessly remove the PEG chains and expose OA, leading to increased cellular uptake in Pan02 cells in an acid environment.

Since the pH-responsive linker can contribute to the increase in cellular uptake and clustering nanoparticles in vitro, we further intravenously injected ZIF@SLN and ZIF@SLN#L (labeled with Cyanine-7) into the Pan02-bearing C57/BL6J mice to study whether the pH-responsive linker can influence the biodistribution of nanoparticles in vivo. As shown in Figure 2E,F, the mice injected with ZIF@SLN#L showed enhanced accumulation than those injected with ZIF@SLN from 0.5 to 24 h post-injection, and the strongest accumulation in mice was ZIF@SLN#L and ZIF@SLN after 6 h. In addition, there was no accumulation in the mice injected with ZIF@SLN#L and ZIF@SLN after 96 h, indicating the elimination of nanoparticles from the mice after this time. Furthermore, the main organs, heart, liver, spleen, lung, kidney, and tumors, were collected from mice injected with ZIF@SLN#L and ZIF@SLN after 6 h. Then the accumulation was quantitatively analyzed in these tissues to study the biodistribution of the nanoparticles (Figure 2G–I). No significant nanoparticles' accumulation in the lung indicated the favorable dispersion of both ZIF@SLN#L and ZIF@SLN in mice circulatory systems.^[38] Additionally, the tumor in mice injected with ZIF@SLN#L displayed higher accumulation than that of mice injected with ZIF@SLN, which was also proved by the quantitative results ($15.9 \pm 1.9\%$ for ZIF@SLN#L and $8.2 \pm 0.9\%$ for ZIF@SLN). These results implied that the pH-responsive linker increases the cellular uptake efficiency on Pan02 cells in vitro and increases the nanoparticle accumulation in the tumor in vivo.

Ap, an old drug developed for the oral treatment of autoimmune conditions, was subsequently discovered as an inhibitor of the lipid kinase enzyme (PIKfyve).^[39] In addition, various studies indicate that PIKfyve inhibitors cause cell death in cancer cell lines, such as A-375 melanoma cells and non-Hodgkin lymphoma, which depend on autophagy for growth and proliferation due to impaired lysosome homeostasis.^[40,41] Interestingly, cancer cells, especially pancreatic cancer cells, are known for high autophagy levels to support the intensified amino acid metabolism and glycometabolism causing malignant proliferation.^[42,43] Given that the acidity of tumors is lower than that of normal tissues,^[44,45] the pH-responsive

linker of Ap-ZIF@SLN#L is expected to promote its accumulation in cancer cells. Therefore, Ap-ZIF@SLN#L is a promising candidate for blocking the autophagy of cancer cells, leading to enhanced intracellular oxidative damage and tumor growth inhibition.

To explore the potential therapeutic effect of Ap-ZIF@SLN#L, the Pan02 cells were cultured with Ap alone, ZIF@SLN#L, and Ap-ZIF@SLN#L at different concentrations and pH values. In Figure 3A,B, when the Pan02 cells were incubated with Ap alone, the cell viability was $\approx 100\%$ without the influence caused by the different concentrations or pH values. In contrast, when the Pan02 cells were incubated with Ap-ZIF@SLN#L (containing 100 nm of Ap), the cell viability was lower than 10% at pH 6.0 and $35.5 \pm 6.8\%$ at pH 7.4. Since the Ap-ZIF@SLN#L decreased the cell viability of Pan02, the effect of Ap-ZIF@SLN#L on normal cells, such as fibroblast and macrophages, was further investigated by evaluating the cell viability. As shown in Figure 3C,D, Ap-ZIF@SLN#L (containing 100 nm of Ap) did not cause a statistically significant decrease in the cell viabilities of both NIH/3T3 and RAW264.7 cells compared to those treated with only cell medium. Lactate dehydrogenase (LDH) and intracellular reactive oxygen species (ROS) assay were assessed on Pan02 cells to study the potential mechanism behind the decreased cell viability. As shown in Figure 3E, increased LDH levels were observed in Pan02 cells treated with Ap alone ($22.7 \pm 1.4\%$), ZIF@SLN#L ($29.1 \pm 3.5\%$), and Ap-ZIF@SLN#L ($37.4 \pm 2.6\%$) at pH 6.0 compared to the Pan02 cells ($11.2 \pm 1.5\%$) without any treatment. Since the increasing level of LDH in serum is usually associated with tissue damage, the increase of LDH in the supernatant of Pan02 cells also indicated cellular damage. The cellular damage was further studied using the dichlorodihydrofluorescein diacetate probe (DCFH-DA) by flow cytometry and confocal fluorescence microscopy. In Figure 3F, after normalizing the DCFH-DA positive events in the Pan02 cells without any treatment, the DCFH-DA positive events in the Pan02 cells treated with Ap alone, ZIF@SLN#L, and Ap-ZIF@SLN#L was $16.7 \pm 6.4\%$, $52.1 \pm 1.8\%$, and $73.2 \pm 5.9\%$, respectively, at pH6.0. In contrast, there were no statistical differences in the DCFH-DA positive events among Pan02 cells treated with Ap alone ($21.5 \pm 12.2\%$), ZIF@SLN#L ($27.8 \pm 10.4\%$), and Ap-ZIF@SLN#L ($24.5 \pm 10.5\%$) at pH 7.4. Noticeably, the DCFH-DA positive events of ZIF@SLN#L at pH 6.0 were higher than at pH 7.4, attributed to the clustering nanoparticles. Moreover, the highest DCFH-DA positive events in Ap-ZIF@SLN#L at pH 6.0 indicate that the clustering nanoparticles and Ap alone can synergistically increase the intracellular ROS level. Furthermore, the intracellular ROS of Pan02 with different treatments are shown in Figure 3G. Correspondingly, higher fluorescence intensity can be observed in the Pan02 cells treated with Ap-ZIF@SLN#L compared to Ap alone and ZIF@SLN#L, consistent with the flow cytometry results. Overall, these results show the potential mechanism of Ap-ZIF@SLN#L in inhibiting the proliferation of Pan02 cells. Under the acid environment, the ZIF@SLN#L part of Ap-ZIF@SLN#L can induce the ROS generation in Pan02 cells; in addition, the released Ap could block the autophagy, leading to a further increased intracellular ROS production, increased LDH levels, and consequently inhibiting the proliferation of Pan02 cells.

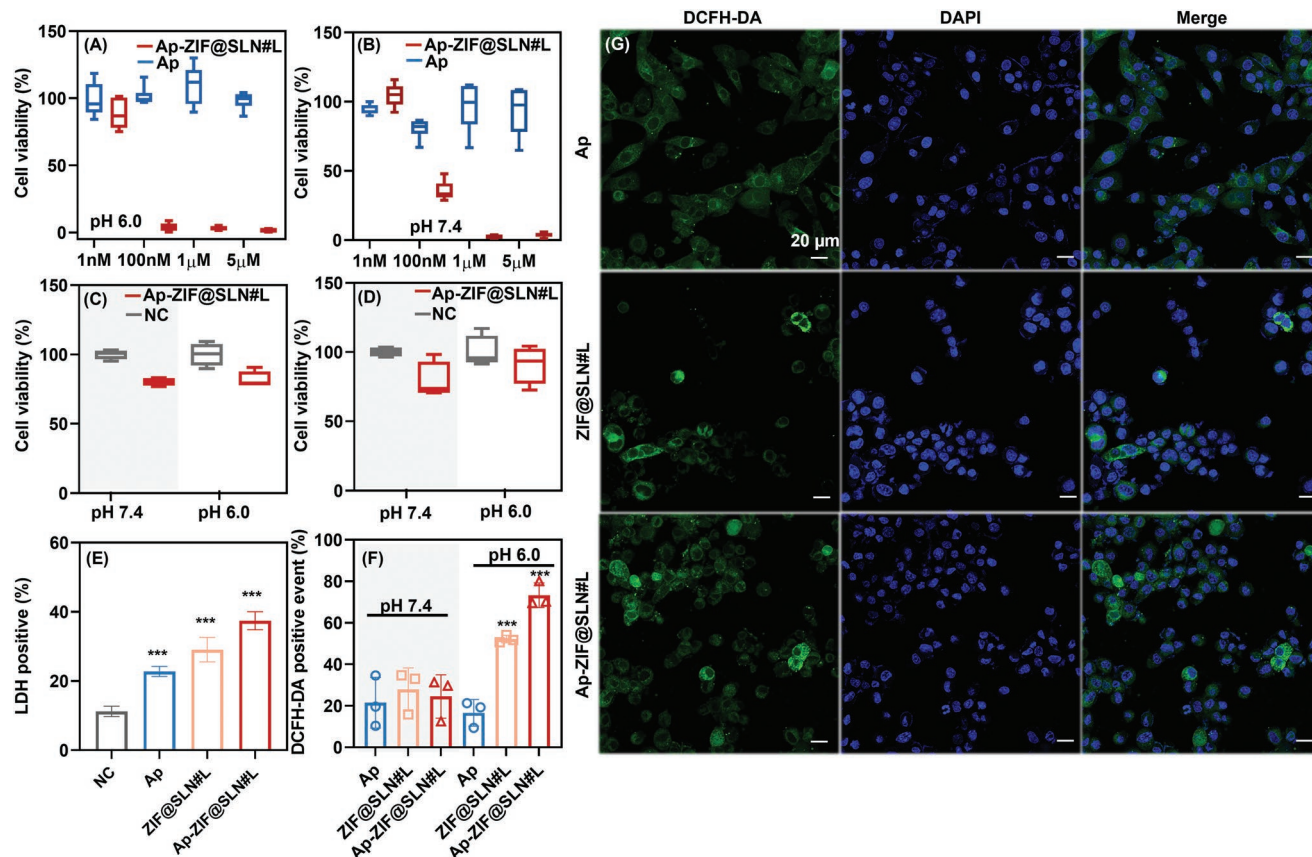


Figure 3. A, B) Cell viability of Pan02 cells cultured with different concentrations of Ap alone and Ap-ZIF@SLN#L at pH 6.0 (A) and pH 7.4 (B); the data were normalized by the cell viability of Pan02 cells cultured without any treatment ($n = 6$). C, D) Cell viability of NIH3T3 (C) and RAW264.7 (D) cultured with Ap-ZIF@SLN#L or without any treatment (denoted as NC) ($n = 4$). E) LDH percentage of Pan02 cells treated with Ap alone, ZIF@SLN#L, and Ap-ZIF@SLN#L or without any treatment (denoted as NC); the data were normalized by the LDH percentage of positive control ($n = 3$). F) Flow cytometry results of DCFH-DA⁺ Pan02 cells treated with Ap alone, ZIF@SLN#L, and Ap-ZIF@SLN#L; the data were normalized by the DCFH-DA⁺ Pan02 cells without any treatment ($n = 3$). G) Confocal fluorescence microscopy images of DCFH-DA⁺ Pan02 cells treated with Ap alone, ZIF@SLN#L, and Ap-ZIF@SLN#L at pH 6.0. Scale bars: 20 μm. The error bars are based on standard errors of the individual cell samples; *** $p < 0.001$, ANOVA with Tukey's post-test.

Encouraged by the obtained results for Ap-ZIF@SLN#L both in vitro and in vivo, we further study the performance of Ap-ZIF@SLN#L in an animal model. First, the 6 weeks old male C57BL/6J mice were subcutaneously injected with Pan02 cells to establish the tumor allograft, followed by removing part of the tumor to mimic the potential post-operative tumor recurrence in clinical (Figure 4A). The tumor was visualized and quantitatively analyzed two days after surgery with an In Vivo Imaging System (IVIS). Mice in each group showed similar average photos per pixel, proving the tumor models were successfully established (Figure 4B,C). Afterward, the mice were intravenously injected with saline, ZIF@SLN#L, Ap alone, and Ap-ZIF@SLN#L every three days since the nanoparticles were eliminated from the tumor of mice after 96 h. After 28 days of treatments, the tumor was visualized and quantitatively analyzed by IVIS. Compared with mice treated with saline, the tumor growth was inhibited in mice treated with ZIF@SLN#L, Ap alone, and Ap-ZIF@SLN#L after 28 days (Figure 4B,D). To further verify the tumor inhibition effect, tumors were isolated from each mouse, and the tumor weights were recorded. The average tumor weight for saline, ZIF@SLN#L, Ap alone, and

Ap-ZIF@SLN#L was 0.62 ± 0.07 , 0.38 ± 0.05 , 0.25 ± 0.03 , and 0.15 ± 0.04 g, respectively (Figure 4E). The mice's body weights increased in all experimental groups without statistical differences, indicating the negligible adverse effects of ZIF@SLN#L, Ap alone, and Ap-ZIF@SLN#L (Figure 4F).

Furthermore, mice in all experimental groups showed similarly organized tissue structures in the heart, liver, spleen, lung, and kidney, according to hematoxylin and eosin stain (H&E stain, Figure S3, Supporting Information). Additionally, the concentration of alanine transaminase and aspartate transaminase in all experimental groups were similar without statistically significant differences among the groups (Figure S4, Supporting Information), suggesting normal liver function in mice. The increased body weight, organized tissue structures, and normal liver function indicate that treatments were not harmful to mice.

Additionally, the Ap-ZIF@SLN#L group showed the highest survival rate (100%) compared to that of saline (0%), ZIF@SLN#L (60%), and Ap (90%) (Figure 4G). Therefore, we further studied the potential mechanism behind the inhibited tumor growth and the increase in the survival rate. As proved

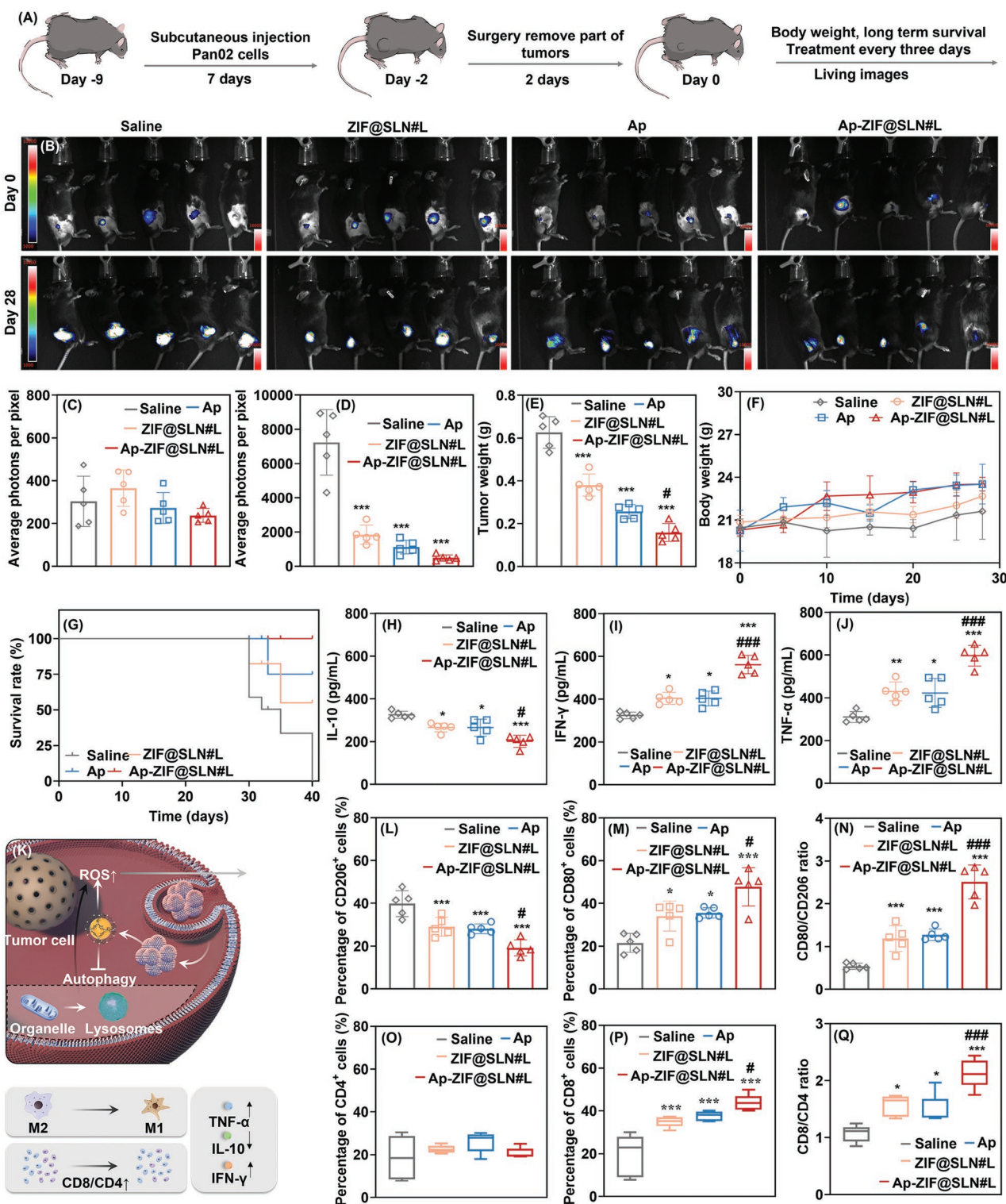


Figure 4. Investigation of Ap-ZIF@SLN#L in the Pan02-bearing mice tumor model. A) Schematic representation of the established tumor model and therapeutic treatments. B) IVIS images of mice from all groups on days 0 and 28, and C,D) quantitative analysis of the IVIS images on day 0 (C) and day 28 (D). E) The tumor weight of mice on day 28 ($n = 5$). F) Body weight of mice ($n = 5$). G) Survival rate of mice ($n = 10$). H–J) Serum concentration of IL-10 (H), IFN- γ (I), and TNF- α (J) in mice ($n = 5$). K) Schematic representation of the potential therapeutic mechanism of the Ap-ZIF@SLN#L in vivo. L,M) Percentages of CD206 $^{+}$ macrophages (L) and CD80 $^{+}$ macrophages (M), and N) the ratio of CD80 $^{+}$ /CD206 $^{+}$ macrophages in mice ($n = 5$). O,P) Percentages of CD4 $^{+}$ T cells (O) and CD8 $^{+}$ T cells (P), and Q) the ratio of CD8 $^{+}$ /CD4 $^{+}$ T cells in mice ($n = 5$). The error bars are based on standard errors of the individual mice. * indicates the statistically significant differences of Ap alone, ZIF@SLN#L, and Ap-ZIF@SLN#L compared with saline. # Statistically significant differences of Ap-ZIF@SLN#L compared with Ap and ZIF@SLN#L. ***, ### $p < 0.001$, ** $p < 0.01$, * $p < 0.05$ ANOVA with Tukey's post-test.

in vitro, the cluster Ap-ZIF@SLN#L nanoparticles can be uptake by cancer cells and other cells, such as macrophages. However, the Ap-ZIF@SLN#L nanoparticles were cytotoxic to cancer cells rather than the normal cells since the cancer cells need a higher level of autophagy to maintain normal functions. Then, after 28 days of treatment, three typical cytokines, interleukin-10 (IL-10), interferon- γ (IFN- γ), and tumor necrosis factors- α (TNF- α), were selected to investigate the potential mechanism. Since previous research indicated that inhibited autophagy could decrease the concentration of IL-10, which is a typical anti-inflammatory cytokine, which can not only inhibit the synthesis of pro-inflammatory cytokines, such as IFN- γ , IL-2, IL-3, and TNF- α but also suppresses the antigen-presentation capacity of antigen-presenting cells.^[46,47] Consequently, the decreased level of IL-10 could increase the level of IFN- γ . IFN- γ can increase the anti-proliferative state in cancer cells and upregulate the expression of MHC I and MHC II with reduced tumor metastasis,^[48,49] and increase the level of TNF- α that is mainly secreted by the macrophages with the potential capability of inducing inflammation and inhibiting tumor growth.^[50,51] In this study, the concentrations of IL-10, IFN- γ , and TNF- α were evaluated in the serum of mice by enzyme-linked immunosorbent assay (ELISA). In Figure 4H–J, the Ap-ZIF@SLN#L group showed the lowest concentration of IL-10 ($201.7 \pm 28.0 \text{ pg mL}^{-1}$) and the highest concentration of IFN- γ ($561.3 \pm 43.0 \text{ pg mL}^{-1}$), and TNF- α ($597.2 \pm 48.3 \text{ pg mL}^{-1}$) compared to the saline, Ap alone, and ZIF@SLN#L.

Since the differentiation of immune cells usually causes the fluctuant concentration of cytokines, we presumed the potential therapeutic mechanism of the Ap-ZIF@SLN#L in vivo (Figure 4K). Therefore, we further chose T cells and macrophages to explore the differentiation of immune cells in vivo. Tumors were isolated and prepared into the single-cell suspension from mice. The cell suspensions were divided into two parallel cell samples, one was stained for analyzing macrophages (Zombie NIR, CD45, CD11b, F4/80, CD80, and CD206), and another one was stained for analyzing T cells (Zombie NIR, CD45, CD3, CD8, and CD4); the gating strategies are presented in Figure S5, (Supporting Information). The Ap-ZIF@SLN#L group showed $19.2 \pm 3.7\%$ CD206⁺ macrophages compared to that of saline ($39.8 \pm 6.1\%$), ZIF@SLN#L ($29.1 \pm 4.4\%$), and Ap ($28.1 \pm 2.3\%$) groups (Figure 4L). In addition, increasing CD80⁺ macrophage was observed in the Ap-ZIF@SLN#L ($47.8 \pm 9.0\%$) group than that in the saline ($21.5 \pm 4.4\%$), ZIF@SLN#L ($34.0 \pm 7.0\%$) and Ap ($35.6 \pm 2.4\%$) groups (Figure 4M). The CD206⁺ is usually regarded as a specific marker for the M2 macrophages contributing to the suppressive TME by secreting cytokines, such as IL-6, IL-8, and IL-10.^[52] In addition, some studies indicate that the CD80⁺ is a marker for the M1 macrophages, which can inhibit tumor progression.^[53,54] Furthermore, the ratio between M1 and M2 macrophages was calculated since there was a potential association between the increased M1/M2 ratio and the activated TME.^[55,56] In Figure 4N, the highest M1/M2 ratio (2.5 ± 0.4) was observed in the Ap-ZIF@SLN#L group than that in the saline (0.5 ± 0.1), ZIF@SLN#L (1.2 ± 0.3) and Ap (1.3 ± 0.1) groups, indicating the polarization from M2 to M1 macrophages in ZIF@SLN#L, Ap alone, and Ap-ZIF@SLN#L groups. Besides macrophages, as another critical immune cell, the differentiation of T cells was

also explored in the CD4⁺ and CD8⁺ subtypes. In Figure 4O, the percentages of CD4⁺ T cells in all groups were similar without statistical differences. Moreover, the highest percentages of CD8⁺ T cells were observed in the ZIF@SLN#L ($35.0 \pm 2.5\%$), Ap ($37.6 \pm 2.3\%$), and Ap-ZIF@SLN#L ($43.7 \pm 3.8\%$) groups than that in the saline ($19.3 \pm 9.8\%$) (Figure 4P). Consequently, a higher CD8⁺/CD4⁺ ratio was calculated in ZIF@SLN#L (1.6 ± 0.2), Ap (1.5 ± 0.3), and Ap-ZIF@SLN#L (2.1 ± 0.3) group than that in the saline (1.1 ± 0.1) (Figure 4Q). The correlation between increased CD8⁺/CD4⁺ ratio and inhibition in tumor growth has also been reported elsewhere.^[57,58]

Encouraged by the obtained results for Ap-ZIF@SLN#L in the Pan02-tumor resection model, we hypothesized that the Ap-ZIF@SLN#L could also exhibit the therapeutic effects in other dense immune suppressive solid tumors, such as breast cancer. Therefore, we further established a 4T1-bearing model in mice to explore the potential therapeutic effect of Ap-ZIF@SLN#L, and investigate whether the Ap-ZIF@SLN#L has the potential capability to treat various solid tumors. (Figure 5A). First, the tumor was visualized and quantitatively analyzed by IVIS at 7 and 28 days after the subcutaneous injection of 4T1 cells on mice (Figure 5B–D). After 7 days, there was no statistically significant difference in each group's average photons per pixel of mice, indicating the successful establishment of a 4T1-bearing tumor model in mice (Figure 5C).

Then the mice were intravenously injected with saline, ZIF@SLN#L, Ap alone, and Ap-ZIF@SLN#L every three days in each group. The body weights of mice were regularly recorded without apparent weight fluctuations (Figure S6, Supporting Information). After 28 days, higher average photons per pixel (4893.1 ± 2660.7) were observed on the mice treated with saline compared to ZIF@SLN#L (1487.3 ± 1442.8), Ap (1055.1 ± 177.8), and Ap-ZIF@SLN#L (513.3 ± 238.9 , Figure 5D). At 28 days, the average tumor volumes for mice treated with saline were $1142.9 \pm 105.7 \text{ mm}^3$, and $691.2 \pm 209.1 \text{ mm}^3$ for ZIF@SLN#L, $531.8 \pm 74.8 \text{ mm}^3$ for Ap, and $218.9 \pm 71.1 \text{ mm}^3$ for the Ap-ZIF@SLN#L (Figure 5E). Additionally, the tumor was isolated and weighted after 28 days. The weight of Ap-ZIF@SLN#L was $0.12 \pm 0.01 \text{ g}$, which was lower than that of saline ($0.52 \pm 0.08 \text{ g}$), ZIF@SLN#L ($0.30 \pm 0.12 \text{ g}$), and Ap ($0.30 \pm 0.12 \text{ g}$, Figure 5F). Furthermore, the tumor was prepared for the single-cell suspension for the following studies. In Figure 5G, representative flow cytometry images of CD8⁺ and CD4⁺ T cells were selected from each group. A significant shift was observed in the population of CD8⁺ T cells from saline to the Ap-ZIF@SLN#L group. The percentages of CD4⁺ and CD8⁺ T cells were similar to that in the Pan02 tumor model (Figure S7, Supporting Information). Moreover, the ratio between CD4⁺ T cells and CD8⁺ T cells was quantified in Figure 5H, showing a similar trend to that of the Pan02 tumor model. The lowest CD4⁺/CD8⁺ ratio was observed in the Ap-ZIF@SLN#L (0.40 ± 0.11) group compared to the saline (1.15 ± 0.11), ZIF@SLN#L (0.73 ± 0.25), and Ap (0.80 ± 0.10) groups. Besides T cells, the population shift of CD206⁺ macrophages was observed by the representative flow cytometry images (Figure 5I). The Ap-ZIF@SLN#L showed the highest percentage of CD80⁺ macrophages ($43.7 \pm 4.3\%$) and the lowest CD206⁺ macrophages ($18.6 \pm 3.8\%$) compared to the other

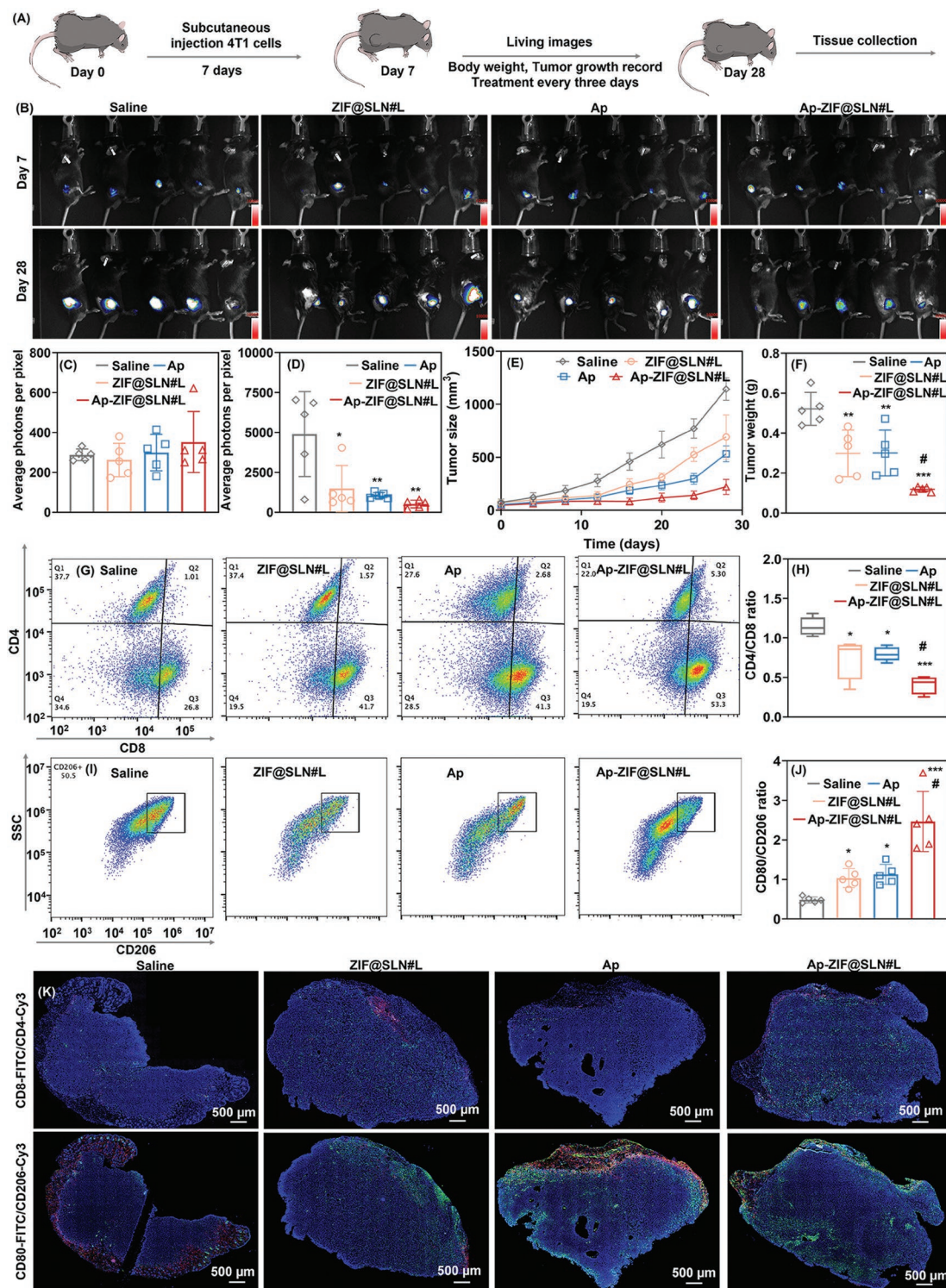


Figure 5. Investigation of Ap-ZIF@SLN#L in a 4T1-bearing mice tumor model. A) Schematic representation of the established tumor model and therapeutic treatments. B) IVIS images of mice from all groups on days 7 and 28, and C,D) quantitative analysis of the IVIS images on day 7 (C) and day 28 (D). E) The tumor volume of mice ($n = 5$). F) Tumor weight of mice ($n = 5$). G) Representative flow cytometry images of CD8⁺ and CD4⁺ T cells from each group, and H) the ratio of CD4⁺/CD8⁺ T cells ($n = 5$). I) Representative flow cytometry images of CD206⁺ and CD80⁺ macrophages from each group, and J) the ratio of CD80⁺/CD206⁺ macrophages ($n = 5$). K) The immunofluorescence images on the tumor tissues from each group. CD4⁺-Cy3 and CD8⁺-FITC co-stained for the T cells, and CD206⁺-Cy3 and CD80⁺-FITC co-stained for the macrophages. Scale bars: 500 μm . The error bars are based on standard errors of individual mice. * indicates the statistically significant difference of Ap alone, ZIF@SLN#L, and Ap-ZIF@SLN#L compared with saline. # Statistically significant difference of Ap-ZIF@SLN#L compared with Ap alone and ZIF@SLN#L. *** $p < 0.001$, ** $p < 0.01$, * $p < 0.05$ ANOVA with Tukey's post-test.

three groups (Figure S8, Supporting Information). Furthermore, the ratios between CD80⁺ and CD206⁺ were calculated in Figure 5J. The highest CD80⁺/CD206⁺ ratio was observed in the Ap-ZIF@SLN#L (2.47 ± 0.76) group compared to the saline (0.48 ± 0.08), ZIF@SLN#L (1.03 ± 0.24), and Ap (1.12 ± 0.25) groups. Encouraged by the increased CD80⁺/CD206⁺ and decreased CD4⁺/CD8⁺ ratio, we further processed the immunofluorescence on the tumor tissues to investigate the infiltration of immune cells (Figure S9, Supporting Information). As shown in Figure 5K, the Ap-ZIF@SLN#L group showed the widespread distribution of CD8⁺T cells, indicating the activating TME. In addition, CD206⁺ macrophages mainly distrusted the tumor boundary with limited CD80⁺ macrophages in the saline group. In contrast, CD80⁺ macrophages mainly distrusted the tumor of ZIF@SLN#L and Ap-ZIF@SLN#L groups. Although, there were numerous CD206⁺ macrophages on the tumor boundary of the Ap group. Unlike the saline group, there were still numerous CD80⁺ macrophages in the Ap group. These immunofluorescence images indicate that the TME is activated by administering Ap-ZIF@SLN#L in the tumor-bearing mice.

3. Conclusion

This work describes the preparation of a pH-responsive cluster MOF nanoparticle to enhance tumor accumulation and the antitumor effect. Ap-ZIF@SLN#L nanoparticle composed of a pH-responsive cluster shell (SLN#L) with ROS-generated core (Ap-ZIF) is reported. Under the acidic TME, ZIF@SLN#L can eliminate both PEG and MMfu parts and expose the OA part, forming the clustering nanoparticles in vitro and vivo. Furthermore, after loading with Ap, the Ap-ZIF@SLN#L inhibits tumor growth by raising the ROS in tumor cells and suppressing the proliferation of tumor cells with favorable biocompatibility, leading to an increased ratio of CD80⁺/CD206⁺ macrophages and CD8⁺/CD4⁺ T cells in both Pan02- and 4T1-tumor-bearing mice. Therefore, the development of Ap-ZIF@SLN#L nanoparticle provides a potential strategy for improving the MOF nanoparticle accumulation in tumors without any active targeting agent and enhancing the antitumor capability by activating the surrounding immune microenvironment in the tumor.

4. Experimental Section

Statistical Analysis: Data were analyzed by SPSS 20 statistical software (version 20.0) using ANOVA with Tukey's post-test used for statistical analysis. For all graphs, error bars indicate mean ± standard deviation for $n \geq 3$ independent experiments (except where noted) and p -values on graphs are denoted within each figure panel as * $p < 0.05$ (significant), ** $p < 0.01$ (moderately significant), and *** $p < 0.001$ (highly significant), respectively. Similarly, *# < 0.05 (significant), **# < 0.01 (moderately significant), and ***# < 0.001 (highly significant), respectively.

Animal Studies: Male C57BL/6J mice (6 weeks) were purchased from Shanghai Jiesijie Laboratory Animal Co., Ltd. The C57BL/6J mice were fed and experiments carried out under protocols approved by Animal Experiment Center, Shanghai Jiaotong University (Number: SYXK2018-0027). The animal experiments were in accordance with international ethics guidelines and the National Institutes of Health Guide, concerning the Care and Use of Laboratory Animals.

Supporting Information

Supporting Information is available from the Wiley Online Library or from the author.

Acknowledgements

This work was supported by grants from the National Key Research and Development Program of China (2020YFA0908200), National Nature Science Foundation of China (81871906, and 82073326, 81871472), and GuangCi Professorship Program of Ruijin Hospital Shanghai Jiao Tong University School of Medicine. Z.L. acknowledges the financial support from the Finnish Red Cross Research Foundation and the Academy of Finland (Grant No. 340129). R.C. acknowledges a China Scholarship Council grant. H.A.S. acknowledges the Sigrid Jusélius Foundation, the Academy of Finland (Grant No. 331151), and UMCG Research Funds for financial support. The authors also acknowledge the following core facilities funded by Biocenter Finland: Electron Microscopy Unit for TEM.

Conflict of Interest

The authors declare no conflict of interest.

Data Availability Statement

The data that support the findings of this study are available from the corresponding author upon reasonable request.

Keywords

cancer, metal–organic frameworks, nanoparticles, pH-responsive targeting, targeting

Received: April 30, 2022
Revised: August 11, 2022
Published online: September 13, 2022

- [1] S. Wang, C. M. McGuirk, A. d'Aquino, J. A. Mason, C. A. Mirkin, *Adv. Mater.* **2018**, *30*, 1800202.
- [2] Y. Sun, L. Zheng, Y. Yang, X. Qian, T. Fu, X. Li, Z. Yang, H. Yan, C. Cui, W. Tan, *Nano-Micro Lett.* **2020**, *12*, 103.
- [3] J. Yang, Y.-W. Yang, *View* **2020**, *1*, 20.
- [4] C. Liu, Q. Sun, L. Lin, J. Wang, C. Zhang, C. Xia, T. Bao, J. Wan, R. Huang, J. Zou, C. Yu, *Nat. Commun.* **2020**, *11*, 4971.
- [5] K. Lu, T. Aung, N. Guo, R. Weichselbaum, W. Lin, *Adv. Mater.* **2018**, *30*, 1707634.
- [6] M.-X. Wu, Y.-W. Yang, *Adv. Mater.* **2017**, *29*, 1606134.
- [7] A. Bieniek, A. P. Terzyk, M. Wiśniewski, K. Roszek, P. Kowalczyk, L. Sarkisov, S. Keskin, K. Kaneko, *Prog. Mater. Sci.* **2021**, *117*, 100743.
- [8] Y. Wang, J. Yan, N. Wen, H. Xiong, S. Cai, Q. He, Y. Hu, D. Peng, Z. Liu, Y. Liu, *Biomaterials* **2020**, *230*, 119619.
- [9] J. Yang, Y.-W. Yang, *Small* **2020**, *16*, 1906846.
- [10] Q. Liu, B. Wu, M. Li, Y. Huang, L. Li, *Adv. Sci.* **2022**, *9*, 2103911.
- [11] X. Wei, N. Li, Y. Wang, Z. Xie, H. Huang, G. Yang, T. Li, X. Qin, S. Li, H. Yang, J. Zhu, F. You, C. Wu, Y. Liu, *Appl. Mater. Today* **2021**, *23*, 100995.
- [12] V. K. LaMer, R. H. Dinegar, *J. Am. Chem. Soc.* **1950**, *72*, 4847.
- [13] J. W. M. Osterrieth, D. Wright, H. Noh, C.-W. Kung, D. Vulpe, A. Li, J. E. Park, R. P. van Duijne, P. Z. Moghadam, J. J. Baumberg, O. K. Farha, D. Fairen-Jimenez, *J. Am. Chem. Soc.* **2019**, *141*, 3893.

- [14] M. J. de Velásquez-Hernández, R. Ricco, F. Carraro, F. T. Limpoco, M. Linares-Moreau, E. Leitner, H. Wiltzsche, J. Rattenberger, H. Schröttner, P. Frühwirt, E. M. Stadler, G. Gescheidt, H. Amenitsch, C. J. Doonan, P. Falcaro, *CrystEngComm* **2019**, *21*, 4538.
- [15] Q. Zhao, Z. Gong, Z. Li, J. Wang, J. Zhang, Z. Zhao, P. Zhang, S. Zheng, R. J. Miron, Q. Yuan, Y. Zhang, *Adv. Mater.* **2021**, *33*, 2100616.
- [16] L. Ding, X. Lin, Z. Lin, Y. Wu, X. Liu, J. Liu, M. Wu, X. Zhang, Y. Zeng, *ACS. Appl. Mater. Interfaces* **2020**, *12*, 36906.
- [17] S. A. Costa, D. Mozdehi, M. J. Dzuricky, F. J. Isaacs, E. M. Brustad, A. Chilkoti, *Nano Lett.* **2019**, *19*, 247.
- [18] A. Tahmasbi Rad, C.-W. Chen, W. Aresh, Y. Xia, P.-S. Lai, M.-P. Nieh, *ACS. Appl. Mater. Interfaces* **2019**, *11*, 10505.
- [19] Z. Cai, F. Xin, Z. Wei, M. Wu, X. Lin, X. Du, G. Chen, D. Zhang, Z. Zhang, X. Liu, C. Yao, *Adv. Healthcare Mater.* **2020**, *9*, 1900996.
- [20] H. Zhang, J. Zhang, Q. Li, A. Song, H. Tian, J. Wang, Z. Li, Y. Luan, *Biomaterials* **2020**, *245*, 119983.
- [21] A. A. Wu, E. Jaffee, V. Lee, *Curr. Oncol. Rep.* **2019**, *21*, 60.
- [22] Y. Liu, N. Qiu, L. Shen, Q. Liu, J. Zhang, Y.-Y. Cheng, K.-H. Lee, L. Huang, *J. Controlled Release* **2020**, *323*, 431.
- [23] M. Yang, J. Li, P. Gu, X. Fan, *Bioact. Mater.* **2021**, *6*, 1973.
- [24] L. Feng, Z. Dong, D. Tao, Y. Zhang, Z. Liu, *Natl. Sci. Rev.* **2018**, *5*, 269.
- [25] K. G. de la Cruz-López, L. J. Castro-Muñoz, D. O. Reyes-Hernández, A. García-Carrancá, J. Manzo-Merino, *Front. Oncol.* **2019**, *9*, 1143.
- [26] V. K. L. Mer, *Ind. Eng. Chem.* **1952**, *44*, 1270.
- [27] Z. Liu, F. Fontana, A. Python, J. T. Hirvonen, H. A. Santos, *Small* **2020**, *16*, 1904673.
- [28] D. Liu, H. Zhang, F. Fontana, J. T. Hirvonen, H. A. Santos, *Lab Chip* **2017**, *17*, 1856.
- [29] D. Liu, H. Zhang, F. Fontana, J. T. Hirvonen, H. A. Santos, *Adv. Drug Delivery Rev.* **2018**, *128*, 54.
- [30] Y. Zhang, D. Liu, H. Zhang, H. A. Santos, in *Microfluidics for Pharmaceutical Applications*, (Eds.: H. A. Santos, D. Liu, H. Zhang), Elsevier, San Diego, CA, USA **2019**, ch. 7.
- [31] S. Feng, M. Bu, J. Pang, W. Fan, L. Fan, H. Zhao, G. Yang, H. Guo, G. Kong, H. Sun, Z. Kang, D. Sun, *J. Membr. Sci.* **2020**, *593*, 117404.
- [32] H. Zhang, M. Zhao, Y. S. Lin, *Microporous Mesoporous Mater.* **2019**, *279*, 201.
- [33] E. J. Luber, M. H. Mobarok, J. M. Buriak, *ACS Nano* **2013**, *7*, 8136.
- [34] D. Cao, X. Shu, D. Zhu, S. Liang, M. Hasan, S. Gong, *Nano Convergence* **2020**, *7*, 14.
- [35] K. Maier, E. Wagner, *J. Am. Chem. Soc.* **2012**, *134*, 10169.
- [36] L.-K. Lin, A. Uzunoglu, L. A. Stanciu, *Small* **2018**, *14*, 1702828.
- [37] T. Shimizu, M. Awata, A. S. Abu Lila, C. Yoshioka, Y. Kawaguchi, H. Ando, Y. Ishima, T. Ishida, *J. Controlled Release* **2021**, *329*, 1046.
- [38] R. Bartucci, A. Paramanandana, Y. L. Boersma, P. Olinga, A. Salvati, *Nanotoxicology* **2020**, *14*, 847.
- [39] O. C. Ikononov, D. Sbrissa, A. Shisheva, *Toxicol. Appl. Pharmacol.* **2019**, *383*, 114771.
- [40] Y. Qiao, J. E. Choi, J. C. Tien, S. A. Simko, T. Rajendiran, J. N. Vo, A. D. Delekta, L. Wang, L. Xiao, N. B. Hodge, P. Desai, S. Mendoza, K. Juckette, A. Xu, T. Soni, F. Su, R. Wang, X. Cao, J. Yu, I. Kryczek, X.-M. Wang, X. Wang, J. Siddiqui, Z. Wang, A. Bernard, E. Fernandez-Salas, N. M. Navone, S. J. Ellison, K. Ding, E.-L. Eskelinen, et al., *Nat. Cancer* **2021**, *2*, 978.
- [41] G. Sharma, C. M. Guardia, A. Roy, A. Vassilev, A. Saric, L. N. Griner, J. Marugan, M. Ferrer, J. S. Bonifacino, M. L. DePamphilis, *Autophagy* **2019**, *15*, 1694.
- [42] S. Yang, X. Wang, G. Contino, M. Liesa, E. Sahin, H. Ying, A. Bause, Y. Li, J. M. Stommel, G. Dell'Antonio, *Genes Dev.* **2011**, *25*, 717.
- [43] H. Xia, D. R. Green, W. Zou, *Nat. Rev. Cancer* **2021**, *21*, 281.
- [44] E. Boedtker, S. F. Pedersen, *Annu. Rev. Physiol.* **2020**, *82*, 103.
- [45] L. Wang, M. Huo, Y. Chen, J. Shi, *Adv. Healthcare Mater.* **2018**, *7*, 1701156.
- [46] K. Kwaśniak, J. Czarnik-Kwaśniak, A. Maziarz, D. Aebisher, K. Zielińska, B. Karczmarek-Borowska, J. Tabarkiewicz, *Cent. Eur. J. Immunol.* **2019**, *44*, 190.
- [47] G. M. Konjević, A. M. Vuletić, K. M. Mirjačić Martinović, A. K. Larsen, V. B. Jurišić, *Cytokine* **2019**, *117*, 30.
- [48] G. Kak, M. Raza, B. K. Tiwari, *Biomol. Concepts* **2018**, *9*, 64.
- [49] D. Jorgovanovic, M. Song, L. Wang, Y. Zhang, *Biomarker Res.* **2020**, *8*, 49.
- [50] G. T. Bardi, M. A. Smith, J. L. Hood, *Cytokine* **2018**, *105*, 63.
- [51] F. Shen, L. Sun, L. Wang, R. Peng, C. Fan, Z. Liu, *Nano Lett.* **2022**, *22*, 4509.
- [52] J. Zhou, Z. Tang, S. Gao, C. Li, Y. Feng, X. Zhou, *Front. Oncol.* **2020**, *10*, 188.
- [53] L. Rao, L. Wu, Z. Liu, R. Tian, G. Yu, Z. Zhou, K. Yang, H.-G. Xiong, A. Zhang, G.-T. Yu, W. Sun, H. Xu, J. Guo, A. Li, H. Chen, Z.-J. Sun, Y.-X. Fu, X. Chen, *Nat. Commun.* **2020**, *11*, 4909.
- [54] Y. Xia, L. Rao, H. Yao, Z. Wang, P. Ning, X. Chen, *Adv. Mater.* **2020**, *32*, 2002054.
- [55] M. Rana, R. Kansal, M. Chaib, B. Teng, M. Morrison, D. N. Hayes, A. G. Stanfill, D. Shibata, J. A. Carson, L. Makowski, E. S. Glazer, *Mol. Carcinog.* **2022**, *6*, 61549.
- [56] M. Oshi, Y. Tokumaru, M. Asaoka, L. Yan, V. Satyananda, R. Matsuyama, N. Matsuhashi, M. Futamura, T. Ishikawa, K. Yoshida, I. Endo, K. Takabe, *Sci. Rep.* **2020**, *10*, 16554.
- [57] L. Munakata, Y. Tanimoto, A. Osa, J. Meng, Y. Haseda, Y. Naito, H. Machiyama, A. Kumanogoh, D. Omata, K. Maruyama, Y. Yoshioka, Y. Okada, S. Koyama, R. Suzuki, T. Aoshi, *J. Controlled Release* **2019**, *313*, 106.
- [58] S. He, J. Li, P. Cheng, Z. Zeng, C. Zhang, H. Duan, K. Pu, *Angew. Chem., Int. Ed.* **2021**, *60*, 19355.